ORIGINAL RESEARCH

Mitochondrial Integrity and Function in the Progression of Early Pressure Overload–Induced Left Ventricular Remodeling

Antoine H. Chaanine, MD; K Sreekumaran Nair, MD, PhD; Robert H. Bergen, III, PhD; Katherine Klaus; Adam J. Guenzel, PhD; Roger J. Hajjar, MD; Margaret M. Redfield, MD

***Background*—**Following pressure overload, compensatory concentric left ventricular remodeling (CR) variably transitions to eccentric remodeling (ER) and systolic dysfunction. Mechanisms responsible for this transition are incompletely understood. Here we leverage phenotypic variability in pressure overload–induced cardiac remodeling to test the hypothesis that altered mitochondrial homeostasis and calcium handling occur early in the transition from CR to ER, before overt systolic dysfunction.

***Methods and Results*—**Sprague Dawley rats were subjected to ascending aortic banding, (n=68) or sham procedure (n=5). At 3 weeks post–ascending aortic banding, all rats showed CR (left ventricular volumes < sham). At 8 weeks post–ascending aortic banding, ejection fraction was increased or preserved but 3 geometric phenotypes were evident despite similar pressure overload severity: persistent CR, mild ER, and moderate ER with left ventricular volumes lower than, similar to, and higher than sham, respectively. Relative to sham, CR and mild ER phenotypes displayed increased phospholamban, S16 phosphorylation, reduced sodium-calcium exchanger expression, and increased mitochondrial biogenesis/content and normal oxidative capacity, whereas moderate ER phenotype displayed decreased p-phospholamban, S16, increased sodium-calcium exchanger expression, similar degree of mitochondrial biogenesis/content, and impaired oxidative capacity with unique activation of mitochondrial autophagy and apoptosis markers (BNIP3 and Bax/Bcl-2).

***Conclusions*—**After pressure overload, mitochondrial biogenesis and function and calcium handling are enhanced in compensatory CR. The transition to mild ER is associated with decrease in mitochondrial biogenesis and content; however, the progression to moderate ER is associated with enhanced mitochondrial autophagy/apoptosis and impaired mitochondrial function and calcium handling, which precede the onset of overt systolic dysfunction. **(*J Am Heart Assoc*. 2017;6:e005869. DOI: 10.1161/JAHA.117.005869.)**

Key Words: heart failure • hypertrophy • mitochondria • remodeling

Heart failure (HF) affects more than 23 million people worldwide[1] and is the leading cause of death in industrialized countries.[2] A history of systemic hypertension is present in a majority of patients who develop HF with preserved or reduced left ventricular ejection fraction (LVEF), and treatment of hypertension potently reduces HF incidence.[3–5] Thus, studies seeking to define the mechanisms leading to HF or to test novel HF therapeutics commonly use rodent models of pressure overload (POL) produced by ascending or transverse aortic banding (AB) as a time-telescoped model of human systemic hypertension or severe aortic stenosis. However, despite the use of inbred rodent strains and analogous to human hypertension and aortic stenosis, there is tremendous phenotypic variability in LV chamber structure and function in AB models.[6–9] Our objective was to leverage this phenotypic variability as a means to gain mechanistic insight into POL-induced LV remodeling. Because maintenance of normal content and function of the mitochondria is critical for cardiac homeostasis, we focused on mitochondrial integrity and function and associated changes in calcium-handling proteins. We hypothesized that phenotypic variability in LV geometry and function in response to POL is associated with differences in severity of POL and in mitochondrial homeostasis. To test this hypothesis, we characterized the spectrum of LV geometric and functional phenotypes over time following a standardized ascending AB (AAB) procedure of intermediate severity in the rat. We then

From the Division of Cardiovascular Diseases (A.H.C., A.J.G., M.M.R.), Division of Endocrinology (K.S.N., K.K.), and Department of Biochemistry and Molecular Biology (R.H.B.), Mayo Clinic, Rochester, MN; Division of Cardiovascular Diseases, Mount Sinai Icahn School of Medicine, New York, NY (R.J.H.).

Correspondence to: Margaret M. Redfield, MD, Division of Cardiovascular Diseases, 200 First St SW, Mayo Clinic, Rochester, MN 55905. E-mail: redfield.margaret@mayo.edu

Received February 13, 2017; accepted May 5, 2017.

Clinical Perspective

What Is New?

- Serial echocardiographic studies of rats subjected to a standardized ascending aortic banding procedure (pressure overload) demonstrated initial concentric left ventricular remodeling in response to pressure overload, but subsequent phenotypic variability in left ventricular remodeling was noted 8 weeks postbanding where persistent concentric left ventricular remodeling was characterized by enhanced mitochondrial biogenesis and function and calcium handling but transition to moderate eccentric remodeling was associated with decreased mitochondrial biogenesis, impaired oxidative capacity, and calcium handling and increased mitochondrial autophagy/apoptosis and extracellular matrix remodeling despite preserved ejection fraction.

What Are the Clinical Implications?

- By demonstrating that impaired mitochondrial activity and homeostasis in response to cardiac stress correlates with adverse changes in left ventricular geometry, diastolic function, and myocardial contractility and efficiency, this study provides evidence to explore additional molecular targets for the development of therapies to enhance mitochondrial function and myocardial energetics and to prevent the progression to overt systolic heart failure.

characterized hemodynamic load, expression, and post-translational modification of calcium-handling proteins, changes in gene expression involved in mitochondrial biogenesis, autophagy and apoptosis, and assessed mitochondrial content and function among the different phenotypes.

Methods

Experimental Model of Ascending Aortic Banding

All procedures involving the handling of animals were approved by the Animal Care and Use Committee of the Mayo Clinic and adhered to the Guide for the Care and Use of Laboratory Animals published by the National Institutes of Health. The AB model was used to generate POL-induced HF. A total of 68 Sprague Dawley rats weighing 180 to 200 g underwent AAB, as previously described in detail.[10] Briefly, animals were sedated by intraperitoneal administration of ketamine (65 mg/kg) plus xylazine (5 mg/kg) and intubated using a 16-gauge catheter and mechanically ventilated with tidal volumes of 2 mL at 50 cycles/min and Fio_2 of 21%. A 1-cm incision was made in the right axilla and the thoracic cage was approached at the level of the second intercostal space. The thymus gland was dissected, then the underlying ascending aorta was separated from the superior vena cava, and a 1-mm (2-mm^2 area) vascular clip was placed around the ascending aorta, right before the right brachiocephalic artery. Rats that underwent a sham surgical procedure, where the aorta was dissected from the superior vena cava but without placement of a clip, were included as controls (sham). Buprenorphine SR (0.6 mg/kg) was administered as a single dose subcutaneously for analgesia after the surgery. The clip size was consistent in all animals. Moreover, the proper placement/position of the clip was verified and clip internalization within the aortic lumen, with aneurysmal growth of the aorta around it, was excluded in all animals at the end of the hemodynamic study after euthanasia of the animal. In previous studies,[11,12] a 1.5-mm^2 size clip resulted in substantial early mortality and a high (but not invariant) rate of progression to eccentric remodeling (ER) and marked systolic dysfunction at 8 weeks post-AAB. Thus, here we utilized a larger clip (2.0 mm^2) to produce less severe POL and a milder phenotype allowing elucidation of differences in phenotypic response to POL.

Based on our previous experience with normal rats, we anticipated little phenotypic variability in normal rats and that 5 rats would constitute an adequate sample size to characterize the sham control rats.[11] Based on our previous experience with the rat AB model using a smaller vascular clip,[11] we anticipated that use of a larger vascular clip would produce slightly less severe POL with lower early mortality but would retain the phenotypical variability we had previously observed but not systematically studied. Thus, a large (n=68) albeit somewhat arbitrary number of rats were subjected to banding. We anticipated that this would provide at least 60 surviving rats to characterize phenotypic variability. Given our experience with the variability in echocardiographic, biochemical, and molecular methodologies used, we anticipated that at least 10 rats per phenotype would be needed to provide adequate statistical power for comparisons across multiple groups.

Echocardiography

Animals underwent transthoracic echocardiography 3 and 8 weeks post-AAB using a vivid 7-echocardiography apparatus with a 14-MHz probe (i13L probe). Animals were sedated with ketamine 80 to 100 mg/kg injected intraperitoneally. Parasternal long and mid-LV (papillary muscle level) short-axis 2-dimensional views were obtained to calculate the LV end-diastolic (LVEDV) and end-systolic (LVESV) volumes as well as the LVEF using the area length formula ($V=5/6\times A\times L$, where V: is the volume in mL, A: is the cross-sectional area of the LV cavity in centimeters squared, obtained from the short-axis image in diastole and in systole, and L: is the diastolic length of the LV cavity in centimeters, measured from the long-axis image as the distance from the endocardial LV apex to the

mitral–aortic junction. From the short-axis view, the thickness of the septum (in centimeters) and the posterior wall (in centimeters) and the LV end-diastolic (LVIDd in centimeters) and LV-end systolic internal diameters (LVIDs in centimeters) were measured from the M-mode image and used to calculate LV fractional shortening (%) as (LVIDd-LVIDs)×100/LVIDd). M-mode images at the level of the aortic valve were obtained to assess left atrial diameter. The LV end-systolic meridional wall stress (10^3 dynes/cm^2) was calculated from the following formula: $0.98\times(0.334\times SAP\times LVIDs)/[LVPWs\times(1+(LVPWs/LVIDs))]-2$ and the LV end-systolic circumferential wall stress (10^3 dynes/cm^2) was calculated from the following formula: $(SAP\times LVIDs)/(2\times LVPWs)\times[(1-LVIDs^3)/(2\times long\ axis^2)\times(LVIDs+LVPWs)]$, where SAP is the systolic arterial pressure in mm Hg and LVPWs is the LV posterior wall thickness in systole in centimeters. Instead of the SAP, LV pressure was used to calculate the LV end-systolic wall stress given the pressure difference between LV and SAP because of AAB.

Invasive Pressure–Volume Loop Measurements of the Left Ventricle

Two days after the 8-week post-AAB echo, animals underwent cardiac catheterization as a terminal procedure. LV pressure–volume (P–V) loop measurements were obtained as previously described.[13] Briefly, rats were anesthetized with inhaled 5% (volume/volume) isoflurane for induction, and subsequently intubated and mechanically ventilated as noted above in the surgery section. Isoflurane was lowered to 2% to 3% (volume/volume) for surgical incision. The chest was opened through a median sternotomy. A 1.9F rat P–V catheter was inserted into the LV apex through an apical stab performed with a 25G needle. Isoflurane was then adjusted (0.5%) to maintain anesthesia and a stable heart rate of ~ 350 bpm. Hemodynamic recordings were performed 5 minutes after stable heart rate using a Scisense P–V Control Unit (FY097B). The intrathoracic inferior vena cava was transiently occluded to decrease venous return during the recording to obtain P–V end-systolic and P–V end-diastolic relationships. Linear fits of the P–V end-systolic relationship were used to calculate the end-systolic elastance slope, and volume intercept (V0) and exponential of the P–V end-diastolic relationship were used to derive the LV stiffness constant (β). To adjust for the degree of LV hypertrophy, we calculated the dimensionless chamber stiffness index by multiplying the P–V end-diastolic relationship by the LV mass. Blood resistivity was measured using a vendor supplied probe. Volume measurements were calculated using the Wei's method from the admittance-acquired data, and pressure sensors were calibrated as per manufacturer's instructions.

Phenotypic Classification

Based on cardiac catheterization data, at week 8 post-AAB, only rats with severe POL (LV maximum pressure >200 mm Hg) were included in the study. In previous and preliminary studies, the AAB model is associated with early concentric remodeling at 3 weeks post-AAB with decreased LVEDV and LVESV relative to sham-operated animals.[9,10,12] Over time, there is subsequent but variable progression to an ER phenotype. Thus, based on the 8 weeks post-AAB echocardiogram, animals were assigned to 1 of 3 phenotypes: (1) persistent concentric remodeling (CR), (2) mild ER (MILD) and (3) moderate ER (MOD), based on the LVEDV and/or LVESV as assessed by echocardiography at week 8 post-AAB and its relationship to the sham group at week 8 post sham procedure. Specifically, the CR phenotype was defined by a LVEDV and/or LVESV that was >20% lower than the average value in sham animals. The mild (MILD) phenotype was defined as a LVEDV and/or LVESV within 20% (higher or lower) of the average in the sham group. The moderate (MOD) remodeling phenotype was defined as a LVEDV and/or LVESV that was >20% higher than the average value in sham. We used the 20% cutoff change in volume as a marker of more significant remodeling as previously described.[14,15]

Reverse Transcription Polymerase Chain Reaction

Total RNA was isolated from mechanically crushed LV tissue using RNeasy Protect Mini kit. Reverse transcription was performed using High Capacity cDNA Reverse Transcription Kits with random oligo-dT priming as followed by the manufacturer's protocols. Polymerase chain reaction (PCR) was performed using an ABI PRISM Sequence Detector System 7500 with SYBR Green as fluorescent, and ROX as a passive reference dye. The PCR primers used were the following: alpha-skeletal muscle actin-F, 5′-tgaagcctcacttcctaccc-3′ and alpha-skeletal muscle actin-R, 5′-cgtcacacatggtgtctagtttc-3′; beta myosin heavy chain (β-MyHC)-F, 5′-caccaacaacccctacgatt-3′ and β-MyHC-R, 5′-agcacatcaaaggcgctatc-3′; brain natriuretic peptide-F, 5′-gtcagtcgcttgggctgt-3′ and brain natriuretic peptide-R, 5′-ccagagctggggaaagaag-3′; collagen I-F, 5′-ccaatggtgctcctggtatt-3′ and collagen I-R, 5′-gttcaccactgttgcctttg-3′; collagen III-F, 5′-caggccaatggcaatgtaaag-3′ and collagen III-R, 5′-gccatcctctagaactgtgtaag-3′; and GAPDH-F, 5′-actcccattcttccacctttg-3′ and 5′-ccctgttgctgtagccatatt-3′.

Mitochondrial DNA was analyzed using a nonquantitative, real-time PCR as previously described.[16] Total DNA was isolated from mechanically crushed LV tissue using QIAamp DNA Mini Kit. PCR was performed using an ABI PRISM Sequence Detector System 7500 with SYBR Green as fluorescent, and ROX as a passive reference dye. The primers

used were the following: TRPM2-F, 5′-agacgggtgagacagctgca ccttttc-3′ and TRPM2-R, 5′-cgagagcatcaagtgcaggcattagag-3′; mitochondrial genome-F, 5′-cctcccattcattatcgccgcccttgc-3′ and mitochondrial genome-R, 5′-gtctgggtctcctagtaggtctgg-gaa-3′.

Western Blotting

Protein extraction was obtained by lysing cells and 20 mg of mechanically crushed LV tissue in a RIPA lysis buffer containing protease inhibitor and phosphatase inhibitor. Protein extracts for Western blotting were obtained by centrifuging at 17949 RCF or G for 10 minutes at 4°C and aspirating the supernatant. Protein concentrations were measured using Bradford protein assay. Twenty micrograms of proteins from each sample were loaded and electrophoresed using SDS-PAGE gels and then transferred to a polyvinylidene difluoride membrane. The membrane was blocked for 1 hour using blocking solution containing 0.15 mol/L sodium chloride, 3 mmol/L potassium chloride, 25 mmol/L Tris-base, 5% skim milk, and 0.05% Tween-20. Blots were incubated with the primary antibody overnight at 4°C. The following primary antibodies were used: GAPDH (1:10 000 dilution), BNIP3 (rodent specific), Bax, Bcl-2, CHOP, cleaved caspase 3 and caspase 3 (1:1000 dilution), sodium-calcium exchanger (NCX-1), matrix metalloproteinase-2 (MMP-2), MMP-9, tissue inhibitor of metalloproteinases-1 (TIMP-1), TIMP-2, and electron transport chain (ETC) complexes cocktail (1/1000 dilution except for ETC cocktail [4/1000 dilution]), Sarcoplasmic/Endoplasmic reticulum Ca(2+) ATPase 2a (SERCA2a), phospholamban, and p-phospholamban, S16 (1:3000 dilution) and Peroxisome proliferator-activated receptor gamma coactivator 1-alpha (PGC-1α) (1:1500 dilution). The second day, after 3 washing steps with Tris-buffered saline-0.05% Tween-20, the blot was incubated with secondary horseradish peroxidase conjugated antibody (1:10 000 dilution) for 45 minutes. The blot was washed 3 times with Tris-buffered saline-0.05% Tween-20; then a super-signal west pico chemiluminescent substrate was used for the detection of protein bands using the film method. Bands densities were quantified using the Photoshop program and were normalized to GAPDH to correct for variations in protein loading.

Measurement of Citrate Synthase and Cytochrome C Oxidase Activity

Citrate synthase (CS) activity was measured from LV tissue lysate according to Srere[17] by use of photospectrometric analyses, absorbance 412 nm, as previously described.[18] Cytochrome C oxidase (COX IV) activity was measured using a Complex IV Rodent Enzyme Activity Microplate Assay Kit by use of photospectrometric analyses, absorbance 550 nm. The kinetics of the enzyme activity was measured every minute at 30°C for 2 hours. Data presented indicate relative COX IV activity among the different groups, which is the slope (OD/min) obtained from the initial linear decrease in absorbance over time. The higher the COX IV activity, the steeper the slope. Protein concentrations in the LV tissue lysate were measured using a commercial kit (Detergent Compatible Protein Assay).

Fibrosis Assessment

Seven-micrometer LV cryosections were stained using the Picrosirius red staining kit. Briefly, slides were fixed in 100% ETOH for 2 minutes and then 50% ETOH for 2 minutes. After 3 washes in deionized water, 3 minutes each, slides were stained with Picrosirius red stain for 1 hour then were washed in 0.5% acetic acid solution twice for 2 minutes. Slides were then dehydrated by ethanol 95% and 100% bath 2 minutes each. After 2 baths of xylene, slides were mounted with Cytoseal 60. 4× and 10× magnification pictures were taken by light microscopy and LV interstitial fibrosis was quantified from the 10×-magnified images using Image J software (NIH). At least 10 fields per animal were quantified from at least 4 animals per group. Also, 4× magnified images were taken by polarized microscopy to assess for the collagen type; yellow: collagen I, and green: collagen III.

Apoptosis by Terminal Deoxynucleotidyl Transferase-Mediated d-UTP-Biotin Nick-End Labeling Assay

Terminal deoxynucleotidyl transferase-mediated d-UTP-biotin nick-end labeling assay was performed using the Apoptag red in situ detection kit and following the protocol provided. Images were acquired at 20× magnification using a Zeiss LSM 780 laser-scanning confocal microscope equipped with a 20× objective. Results were quantified using Image J software (NIH). At least 10 fields per animal were quantified from at least 5 animals per group.

Statistical Analysis

Results are shown as mean±SD. Statistical significance was determined using 1-way ANOVA with multiple comparisons followed by Bonferroni correction across all study groups (sham and the 3 phenotypes). All presented P values are Bonferroni-adjusted P values with a value <0.05 considered significant. Additionally, the ordinary 1-way ANOVA *post-test for linear trend* was applied to the 3 remodeling phenotypes to assess the presence or absence of a directionally similar and progressive change across the 3 remodeling phenotypes. Graph Pad—Prism software was used to perform the statistical analysis.

Results

A total of 68 animals were subjected to AAB. Ten animals died suddenly (3 at <7 days postbanding) and 4 were euthanized because of distress related to large aortic aneurysm (1×1 cm) formation before study end. Eight weeks after AAB, 15 rats had nonsevere POL (LV maximum pressure <200 mm Hg) because of clip displacement, internalization of the clip within the aortic wall, or small aneurysm formation in the periclip region and therefore were excluded (Table 1). Among the rats with severe POL, at 8 weeks post-AAB, 11 met criteria for the CR phenotype, 14 for the MILD phenotype, and 14 for the MOD phenotype.

Echocardiography at Week 3 Post-AAB

At the 3-weeks post-AAB echo, all phenotypes displayed a CR phenotype with smaller LV volumes, Figure 1A and B, and increased LVEF (Table 2) compared with sham animals. There was a modest linear trend for larger LV volumes and lower LVEF across the 3 phenotypes (*P* for trend 0.02–0.04).

Phenotypic Assessment at Week 8 Post-AAB

By definition, LV volumes varied according to phenotype and in relation to sham animals at week 8 post-AAB (Figure 1C and D and Table 3). Representative M-mode images of the different phenotypes at the midpapillary muscle are presented in Figure 2A. At 8 weeks, LV wall thickness was greater than sham in all remodeling phenotypes (Figure 2B and C). The relative wall thickness and LV mass/volume ratio were increased relative to sham in all 3 remodeling phenotypes but decreased progressively across the 3 phenotypes (*P* for trend <0.006 for both) (Table 3).

Table 1. Echocardiography Parameters of the Excluded Rats That Did Not Develop Severe POL

Groups	Rats With LVPmax <200 mm Hg (n=15)
BW, g	457±44
IVSd, cm	0.22±0.02
LVPWd, cm	0.22±0.02
LVEDV, μL	598±145
LVESV, μL	99±23
LVEF, %	83±3
LVPmax, mm Hg	159±32

Data presented are mean±SD. BW indicates body weight; IVSd, interventricular septal thickness in end-diastole; LVEDV, left ventricular end-diastolic volume; LVEF, left ventricular ejection fraction; LVESV, left ventricular end-systolic volume; LVPmax, maximum left ventricular pressure; LVPWd, left ventricular wall thickness in end-diastole; POL, pressure overload.

Meridional LV end-systolic wall stress was decreased relative to sham in the CR and MILD, but not in the MOD phenotypes. Circumferential LV end-systolic wall stress was decreased relative to sham in the CR, but not in MILD phenotype and was higher than sham in the MOD phenotype (Table 3). Both end-systolic wall stresses increased progressively across the 3 phenotypes (*P* for trend <0.0001 for both). The LVEF was greater than sham in the CR and MILD, but not in MOD, phenotypes (Figure 2D and Table 3).

At autopsy, the heart and LV to body weight ratios in the 3 remodeling phenotypes were significantly higher than sham and increased progressively across the 3 phenotypes (*P* for trend <0.005 for both). The RV weight to body weight ratio was higher than sham in the MOD phenotype only (Table 3).

Representative P–V loop tracings at baseline and during inferior vena cava occlusion of the different phenotypes are presented in Figure 3A. Heart rates were similar to sham and similar across phenotypes (Table 4). The LV maximum pressure was higher than sham in all remodeling phenotypes but similar among phenotypes (Figure 3B). The LV end diastolic pressure was increased relative to sham in the MILD and MOD phenotypes (Figure 3C). The LV diastolic stiffness constant (β) and the dimensionless chamber stiffness index were significantly higher in all remodeling phenotypes relative to sham, and were higher in the MOD phenotype compared with CR and MILD phenotypes (Table 4 and Figure 3D). LV end-systolic elastance and end-systolic elastance/arterial elastance ratio, as measures of LV contractility and efficiency, were higher in the CR and MILD, but not MOD, phenotypes compared with sham (Figure 3E and Table 4). LV end diastolic pressure progressively increased while LV contractility and efficiency progressively decreased across the 3 phenotypes (*P* for trend <0.007 for all) (Table 4).

LV interstitial fibrosis (light microscopy) and collagen I protein (polarized microscopy) and mRNA expression (real-time PCR) were increased in all remodeling phenotypes relative to sham and were higher in the MOD phenotype compared with the CR and MILD phenotypes (Figure 4A through C). Compared with sham, collagen III mRNA expression was significantly increased in the CR phenotype only, with trends (*P*=0.293 and 0.089) towards increases in the MILD and MOD phenotypes, Figure 4D.

The mRNA expression of alpha-skeletal muscle actin was similarly increased in all phenotypes compared with sham (Figure 4E). The mRNA expression of β-myosin heavy chain and brain natriuretic peptide were increased relative to sham and were higher in the MOD phenotype compared with the CR and MILD phenotypes (Figure 4F and G).

Matrix Metalloproteinases

Given that the extracellular matrix was severely remodeled in the MOD phenotype, more so than the CR and MILD

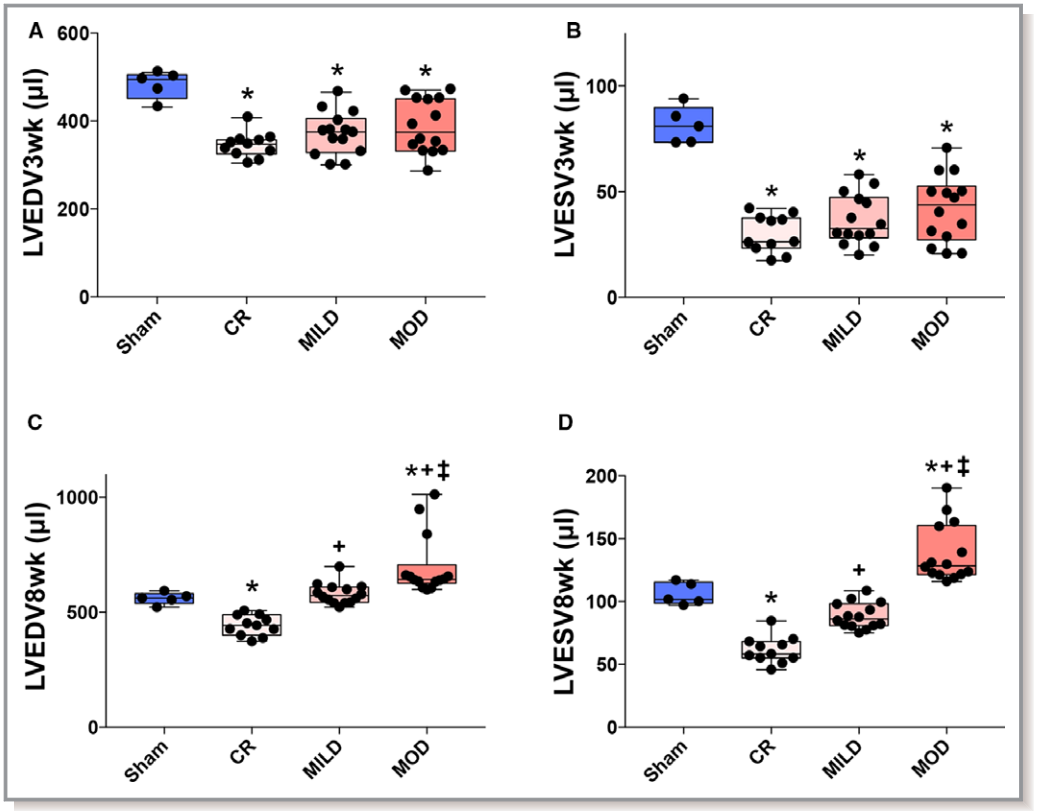

Figure 1. Serial assessment of LV volumes at 3 and 8 weeks post-ascending aortic banding (AAB) in the different phenotypes. LV end-diastolic (LVEDV) and LV end-systolic (LVESV) volume at 3 (A and B) and 8 (C and D) weeks post-AAB. Individual data points, box and whisker plots showing the median, interquartile range, and maximum and minimum values. **P*<0.05 vs sham; $^{+}$*P*<0.05 vs CR and ‡*P*<0.05 vs MILD. CR indicates concentric remodeling; MILD, mild eccentric remodeling; MOD, moderate eccentric remodeling.

phenotypes, we sought to check for the expression of the MMPs, particularly the gelatinases MMP-2 and MMP-9 and the tissue inhibitors of MMPs, TIMP-1, and TIMP-2, which have been shown to play a role in myocardial diastolic stiffening and remodeling.[19–23] Immunoblotting showed increase in MMP-2 expression in the CR and MILD phenotypes compared with sham and was further increased in the MOD phenotype compared with sham, CR, and MILD. Furthermore, there was increase in the dimerization of MMP-2 in the MOD phenotype, which has been shown to correlate with increased MMP-2 activity[24] (Figure 5A). MMP-9 expression was increased and TIMP-1 expression was decreased in the MOD phenotype only (Figure 5A). There was a trend in increased TIMP-2 expression in the CR, MILD, and MOD phenotypes, but did not reach significance compared with sham (Figure 5A). The normalization of MMP-2 and MMP-9 expression to TIMP-1 expression showed robust increases in MMP-2 and MMP-9/TIMP-1 ratios in the MOD phenotype only, suggesting a higher MMP activity in this phenotype. This was not the case when the ratios of MMP-2 and MMP-9 over TIMP-2 were obtained (Figure 5B).

Calcium Cycling Proteins

There was no significant difference in SERCA2a expression between the different remodeling phenotypes and the sham group (Figure 6A). Changes in other calcium-handling proteins were altered in a nonlinear fashion across the phenotypes. Expression of the NCX-1 was lower while phosphorylation of phospholamban at S16 was higher in CR and MILD phenotypes compared with sham. However, in the MOD phenotype, expression of NCX-1 was increased and phosphorylation of phospholamban at S16 was decreased relative to sham and the other phenotypes (Figure 6A). While LVEF was preserved in the MOD phenotype, increases in NCX-1 and decreased phospholamban phosphorylation are characteristic of humans with and experimental models of overt systolic HF.[25–29]

Endoplasmic Reticulum and Mitochondrial Homeostasis

Expression of the endoplasmic reticulum stress apoptotic marker, CHOP, was numerically but not significantly higher than sham in the different phenotypes (Figure 6B). Of the other markers of endoplasmic reticulum stress, we looked at

Table 2. Echocardiographic Parameters in the Different Phenotypes at Week 3 Post-AAB

Groups	BW (g)	IVSd (cm)	LVPWd (cm)	LVEDV (μL)	LVESV (μL)	LVEF (%)
Sham (n=5)	320±7	0.17±0.01	0.18±0.01	481±32	81±9	83±2
CR (n=11)	298±11	0.26±0.02*	0.26±0.02*	344±28*	30±9*	91±3*
MILD (n=14)	314±22	0.26±0.01*	0.26±0.01*	371±48*	37±12*	90±3*
MOD (n=14)	311±21	0.26±0.01*	0.26±0.02*	395±77*	49±28*	88±5*
ANOVA *P*	*P*=0.1325	*P*=0.8168	*P*=0.9500	*P*=0.0998	*P*=0.0466	*P*=0.0960
Post-test for linear trend†	*P*=0.1033	*P*=0.5685	*P*=0.8867	*P*=0.0331	*P*=0.0168	*P*=0.0371

Data presented are mean±SD. AAB indicates ascending aortic banding; BW, body weight; CR, concentric remodeling; IVSd, interventricular septal thickness in end-diastole; LVEDV, left ventricular end-diastolic volume; LVEF, left ventricular ejection fraction; LVESV, left ventricular end-systolic volume; LVPWd, left ventricular wall thickness in end-diastole; MILD, mild eccentric remodeling; MOD, moderate eccentric remodeling.

*$P<0.05$ vs sham.

†Post-test for linear trend across the 3 remodeling phenotypes (not including the sham group).

CHOP because it has been shown to modify protein translation and mediate endoplasmic reticulum–initiated cell death. Its ablation has been shown to be protective against POL-induced hypertrophy and HF.[30] The expression of the mitochondrial death and mitophagy marker, BNIP3, and the Bax/Bcl-2 ratio, a marker of increased mitochondrial apoptosis, were uniquely increased in the MOD phenotype as compared with sham (and the CR and MILD phenotypes) (Figure 6C). Similarly, apoptosis, both by TUNEL assay and immunoblotting for cleaved caspase 3, was uniquely increased in the MOD phenotype compared with sham and the CR and MILD phenotypes (Figure 7A and B).

Table 3. Echocardiographic and Autopsy Parameters of the Different Phenotypes 8 Weeks Post-AAB

Groups	Sham (n=5)	CR (n=11)	MILD (n=14)	MOD (n=14)	ANOVA *P*	Post-Test for Linear Trend§
BW, g	540±37	497±43	530±59	553±68	*P*=0.0777	*P*=0.8354
IVSd, cm	0.19±0.01	0.29±0.01*	0.28±0.02*	0.28±0.01*	*P*=0.3122	*P*=0.1499
LVPWd, cm	0.2±0.01	0.29±0.02*	0.28±0.02*	0.28±0.01*	*P*=0.6077	*P*=0.3259
LVEDV, μL	561±26	442±42*	583±45†	697±129*,†,‡	*P*<0.0001	*P*<0.0001
LVESV, μL	106±9	59±7*	85±11†	140±23*,†,‡	*P*<0.0001	*P*<0.0001
LVEF, %	81±1	87±2*	85±2*	80±2†,‡	*P*<0.0001	*P*<0.0001
RWT, %	0.56±0.03	1.03±0.11*	0.90±0.09*,†	0.77±0.09*,†	*P*<0.0001	*P*<0.0001
HW, mg	1269±125	1645±191*	1821±169*	2106±292*,†,‡	*P*<0.0001	*P*<0.0001
LVW, mg	897±94	1222±152*	1372±135*	1580±219*,†,‡	*P*<0.0001	*P*<0.0001
RVW, mg	218±22	239±26	249±26	283±42*,†,‡	*P*=0.0038	*P*=0.0019
HW/BW, mg/g	2.35±0.13	3.31±0.21*	3.41±0.20*	3.75±0.54*,†	*P*<0.0099	*P*=0.0045
LVW/BW, mg/g	1.66±0.11	2.46±0.20*	2.57±0.16*	2.81±0.35*,†	*P*<0.0039	*P*=0.0014
RVW/BW, mg/g	0.40±0.02	0.48±0.03	0.47±0.03	0.51±0.09*	*P*=0.2356	*P*=0.3045
Meridional wall stress, 10^3 dynes/cm^2	10.82±1.52	1.86±0.66*	4.09±0.28*,†	10.51±5.19†,‡	*P*<0.0001	*P*<0.0001
Circumferential wall stress, 10^3 dynes/cm^2	168±16	102±14*	170±14†	286±121*,†,‡	*P*<0.0001	*P*<0.0001
Mass/volume, g/mL	1.59±0.15	2.79±0.46*	2.37±0.22*,†	2.23±0.59*,†	*P*=0.0114	*P*=0.0057

Data presented are mean±SD. AAB indicates ascending aortic banding; BW, body weight; CR, concentric remodeling; HW, heart weight; IVSd, interventricular septal thickness in end-diastole; LVEDV, left ventricular end-diastolic volume; LVEF, left ventricular ejection fraction; LVESV, left ventricular end-systolic volume; LVPWd, left ventricular wall thickness in end-diastole; LVW, left ventricular weight; MILD, mild eccentric remodeling; MOD, moderate eccentric remodeling; RVW, right ventricular weight; RWT, relative wall thickness.

*$P<0.05$ vs sham.

†$P<0.05$ vs CR.

‡$P<0.05$ vs MILD.

§Post-test for linear trend across the 3 remodeling phenotypes (not including the sham group).

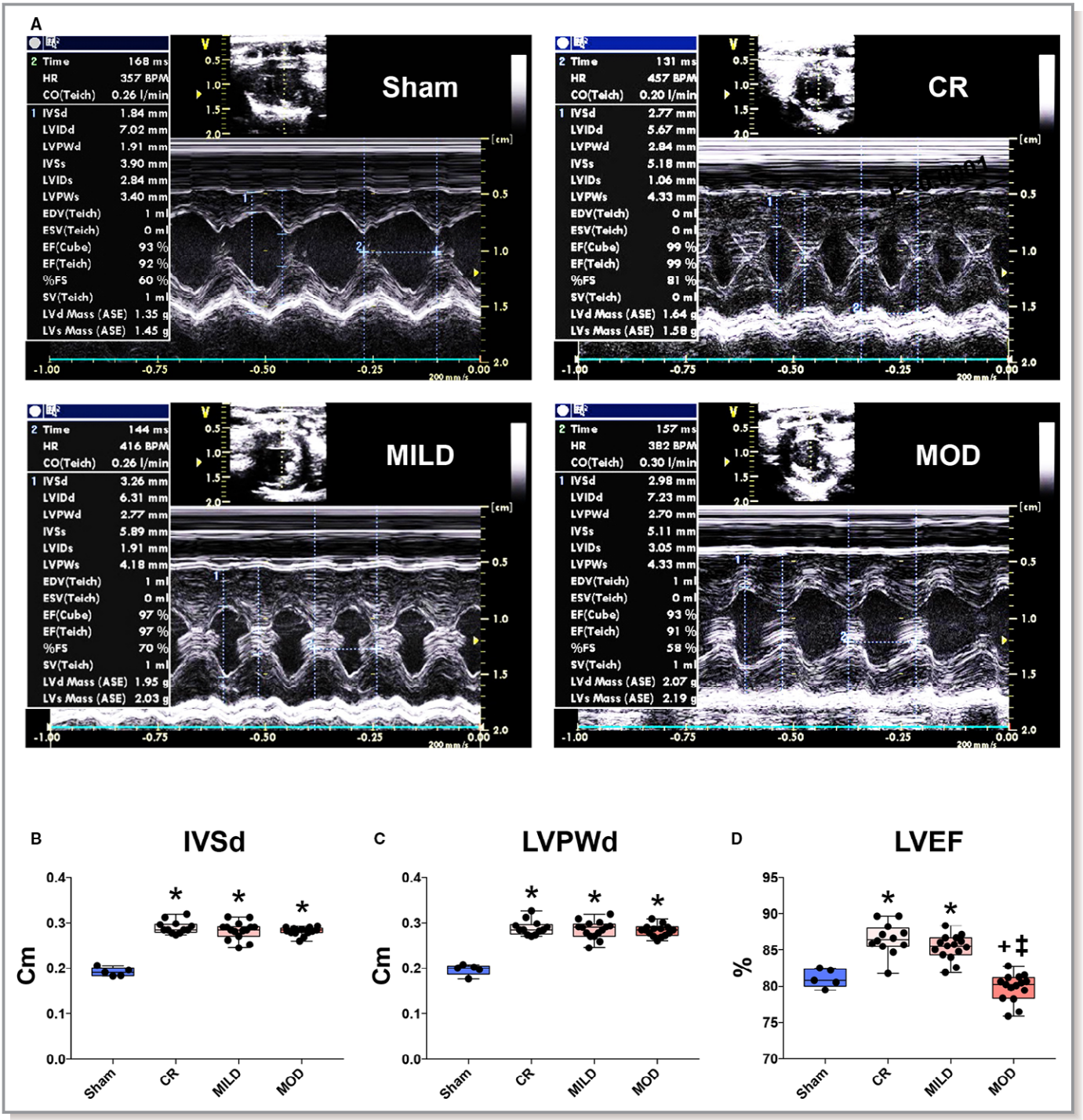

Figure 2. Echocardiographic assessment of the different phenotypes. A, Representative M-mode images at the level of the midpapillary muscle in the different phenotypes. B and C, LV septal (IVSd) and posterior wall (LVPWd) thickness across the different phenotypes. D, LV ejection fraction (LVEF) across the different phenotypes. Individual data points, box and whisker plots showing the median, interquartile range, and maximum and minimum values. **P*<0.05 vs sham; †*P*<0.05 vs CR and ‡*P*<0.05 vs MILD. CR indicates concentric remodeling; IVSd, interventricular septal thickness in end-diastole; LVEF, left ventricular ejection fraction; LVPWd, left ventricular wall thickness in end-diastole; MILD, mild eccentric remodeling; MOD, moderate eccentric remodeling.

Immunoblotting analysis of LV tissue lysates for the ETC complexes showed increases in complex I and complex IV expression in the CR and MILD phenotypes compared with sham, while the MOD phenotype had lower expression of these complexes compared with sham (and the CR and MILD phenotypes) (Figure 8A). Similarly, COX IV was uniquely decreased in the MOD phenotype as compared with sham, CR, and MILD phenotypes (Figure 8C). In contrast, CS activity,

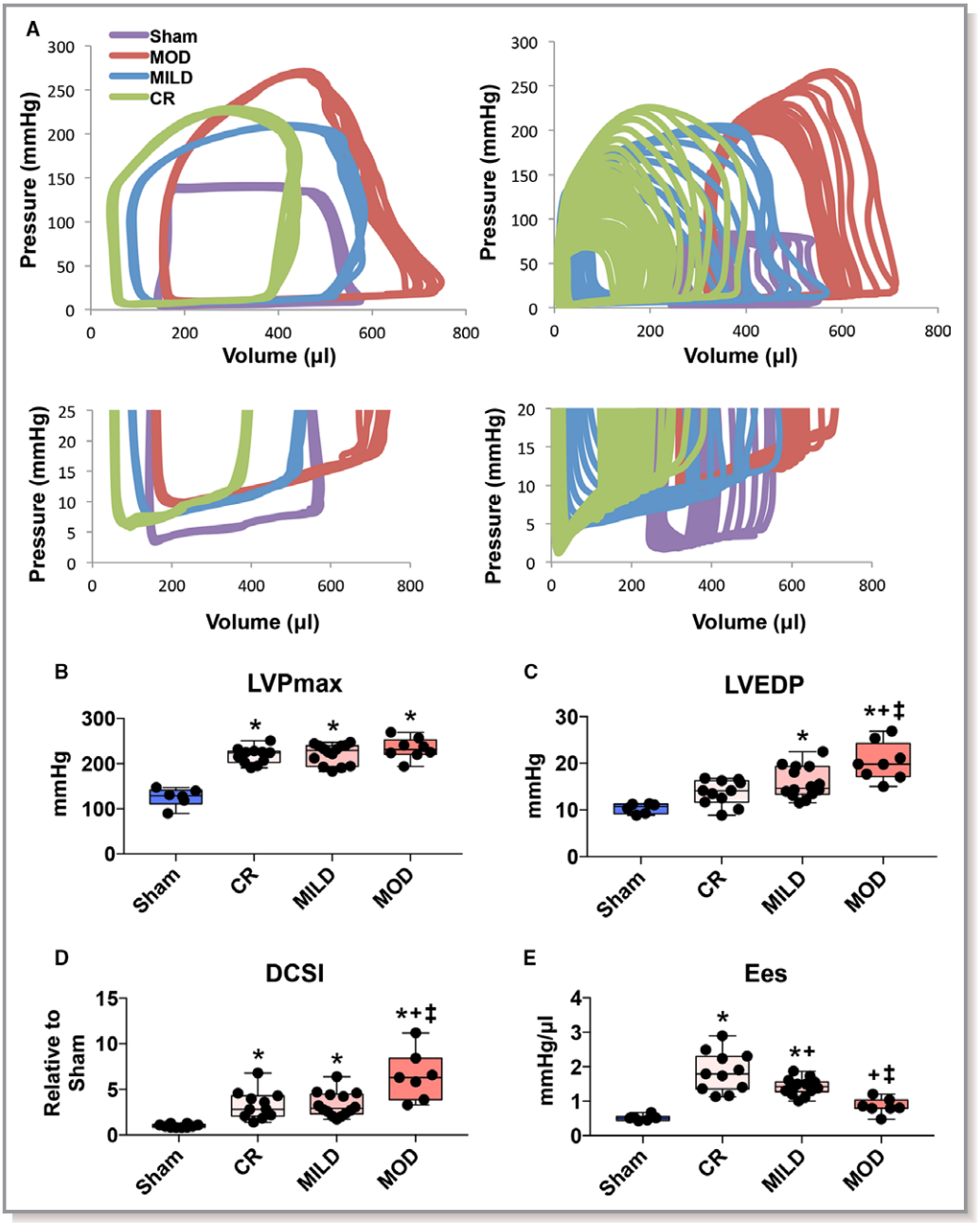

Figure 3. Hemodynamic assessment of the different phenotypes. A, Top panel: Representative P–V loop tracings at steady state (left) and with inferior vena cava constriction (right) in the different phenotypes. Bottom panel: Representative P–V loop tracings scaled for diastolic pressures at steady state (left) and with inferior vena cava constriction (right) in the different phenotypes. LV maximum pressure (LVPmax) (B), LV end-diastolic pressure (LVEDP) (C), the dimensionless chamber stiffness index (DCSI) (D) and end-systolic elastance (Ees) (E) across the different phenotypes. Individual data points, box and whisker plots showing the median, interquartile range, and maximum and minimum values. **P*<0.05 vs sham; $^{+}$*P*<0.05 vs CR and ‡*P*<0.05 vs MILD. CR indicates concentric remodeling; LV, left ventricular; MILD, mild eccentric remodeling; MOD, moderate eccentric remodeling; P–V, pressure–volume.

a marker of Krebs cycle activity, was increased relative to sham in the MILD and MOD phenotypes, and increased progressively (*P* for trend =0.0003) across the remodeling groups (Figure 8B). The expression of the mitochondrial biogenesis marker, PGC-1α, and the mitochondrial/nuclear DNA ratio, a marker of mitochondrial content, were significantly increased in the CR and MILD, but not in the MOD, phenotypes compared with sham, with progressive decrease across the 3 phenotypes (*P* for trend <0.0001) (Figure 8D and E).

Table 4. Hemodynamic Parameters of the Different Groups 8 Weeks Post-AAB

Groups	HR (bpm)	LVPmax (mm Hg)	LVEDP (mm Hg)	β (mm Hg/μL)	DCSI Relative to Sham	Ees (mm Hg/μL)	Ees/Ea
Sham (n=5)	353±43	126±20	10.35±1.1	0.018±0.004	0.99±0.23	0.51±0.09	1.54±0.60
CR (n=11)	349±60	218±16*	13.7±2.7	0.043±0.017*	3.29±1.57*	1.86±0.58*	3.35±1.23*
MILD (n=14)	332±40	221±19*	15.9±3.3*	0.039±0.015*	3.34±1.33*	1.42±0.24*,†	2.62±0.55*
MOD (n=8)	337±48	233±23*	20.3±4.1*,†,‡	0.067±0.023*,†,‡	6.49±2.69*,†,‡	0.85±0.23†,‡	1.83±0.41†,‡
ANOVA *P*	*P*=0.6716	*P*=0.2791	*P*=0.0007	*P*=0.0049	*P*=0.0011	*P*<0.0001	*P*=0.0028
Post-test for linear trend§	*P*=0.5794	*P*=0.1260	*P*=0.0002	*P*=0.0069	*P*=0.0008	*P*<0.0001	*P*=0.0007

Data presented are mean±SD. AAB indicates ascending aortic banding; CR, concentric remodeling; DCSI, indicates dimensionless chamber stiffness index; Ees, end-systolic elastance; Ea, arterial elastance; HR, heart rate; LVEDP, LV end-diastolic pressure; LVPmax, maximum LV pressure; MILD, mild eccentric remodeling; MOD, moderate eccentric remodeling; β, the diastolic stiffness coefficient.

*$P<0.05$ vs sham.

†$P<0.05$ vs CR.

‡$P<0.05$ vs MILD.

§Post-test for linear trend across the 3 remodeling phenotypes (not including the sham group).

Discussion

At 3 weeks after POL produced by a standardized AAB procedure in the rat, all animals displayed CR. However, by 8 weeks post-AAB and despite similar LV systolic pressure, 3 LV remodeling phenotypes were apparent with LV volumes smaller than, similar to, or greater than sham indicating persistent CR (CR) or mild (MILD) to moderate (MOD) ER. The energetic demand (LV end-systolic wall stress) increased progressively across the 3 phenotypes. LVEF, a relatively load-insensitive measure of LV contractility (end-systolic elastance) and LV efficiency, was enhanced in the CR and MILD phenotypes and decreased progressively across the 3 phenotypes. LV filling pressures were increased in the MILD and MOD phenotypes relative to sham and increased progressively across the 3 phenotypes. LV diastolic stiffness was increased in all phenotypes and most strikingly in the MOD phenotype. Similarly, fetal gene expression and interstitial fibrosis in the LV myocardium were increased in all phenotypes and most strikingly in the MOD phenotype. Moreover, MMP-2 and MMP-9 expression was increased, but more importantly, TIMP-1 expression was robustly decreased in the MOD phenotype, suggesting robust increases in MMP-2 and MMP-9 activities and extracellular matrix remodeling in this phenotype and as previously shown.[20–22] These data further highlight the important role of TIMP-1 as a nodal modulator of MMPs activity, extracellular matrix and myocardial remodeling, at least in this model of HF and similar to what has been shown in human HF.[19]

While there was no significant difference in SERCA2a expression across the phenotypes, phospholamban S16 phosphorylation, and therefore SERCA2a activity, was increased in the CR and MILD phenotypes but decreased in the MOD phenotype relative to sham. Similarly, relative to sham, NCX-1 expression was decreased in the CR and MILD phenotypes but increased in the MOD phenotype. As compared with sham, mitochondrial biogenesis (PGC-1α) and mitochondrial content were increased in CR and MILD but not the MOD phenotype where markers of mitochondrial autophagy (BNIP3) and apoptosis (BNIP3 and Bax) were uniquely activated. Moreover, cleaved caspase 3 was increased and evidence of enhanced myocyte loss was validated by TUNEL assay in the MOD phenotype.

Mitochondrial biogenesis and content decreased progressively across the 3 phenotypes. Relative to sham, CS activity was increased in the MILD and MOD phenotypes and increased progressively across the 3 phenotypes. However, complex I and complex IV expression increased in the CR and MILD phenotypes and decreased along with COX IV activity in the MOD phenotype. This suggests mitochondrial oxidative phosphorylation uncoupling between the Krebs cycle and ETC and decreased oxidative capacity in the MOD phenotype. These findings suggest enhanced mitochondrial biogenesis and function in compensatory hypertrophy followed by impairment (relative to demand) in mitochondrial homeostasis, mitochondrial function, and calcium handling early in the transition and progression from compensatory POL hypertrophy to pathologic ER and before the development of overt systolic dysfunction.

Previous studies have identified differences in band severity because of inadequate band standardization, band internalization, or periband aortic remodeling[8] as a critical factor accounting for phenotypic variability following AB.[9] We used a standard size vascular clip rather than a stitch to produce banding, prespecified the presence of significant POL for study entry, and did not find significant differences in POL (as assessed by LV systolic pressure) across the different phenotypes. While sex and rodent strain[6,7,31] are recognized to

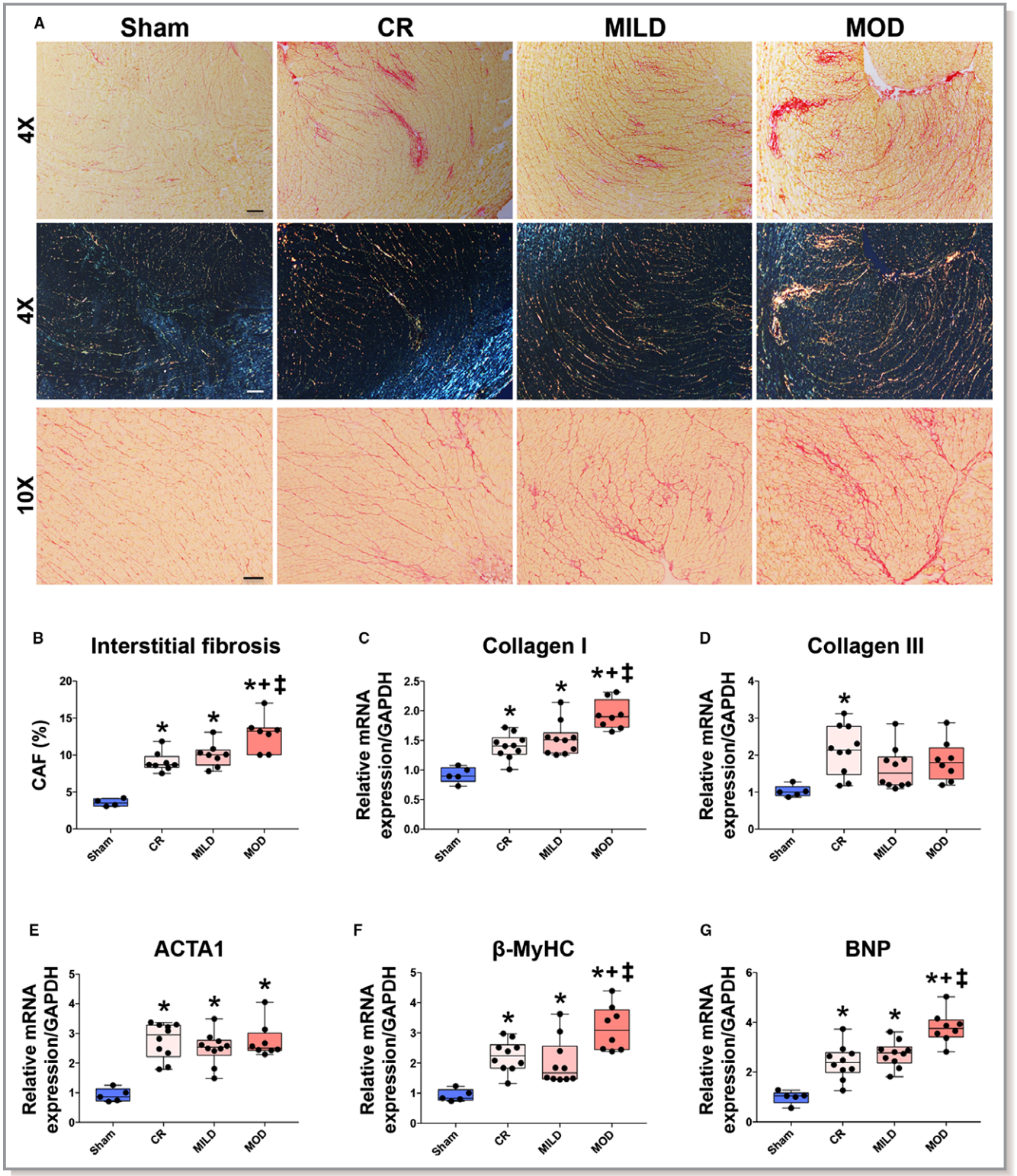

Figure 4. LV interstitial fibrosis, markers of pathological hypertrophy and fetal gene expression in the different phenotypes. A, Representative photomicrographs of LV tissue stained with Picrosirius red taken by light (upper and bottom row) and polarized microscopy (middle row). Upper and middle row scale bar 200 μm. Bottom row scale bar 100 μm. B, Interstitial fibrosis assessed by collagen area fraction (CAF). C and D, Collagen I and III mRNA expression relative to sham. E, F, and G, Alpha-skeletal muscle actin (ACTA1), Beta-myosin heavy chain (β-MyHC) and brain natriuretic peptide (BNP) mRNA expression relative to sham. Individual data points, box and whisker plots showing the median, interquartile range, and maximum and minimum values. *P<0.05 vs sham; ^{+}P<0.05 vs CR and $^{‡}P$<0.05 vs MILD. CR indicates concentric remodeling; MILD, mild eccentric remodeling; MOD, moderate eccentric remodeling.

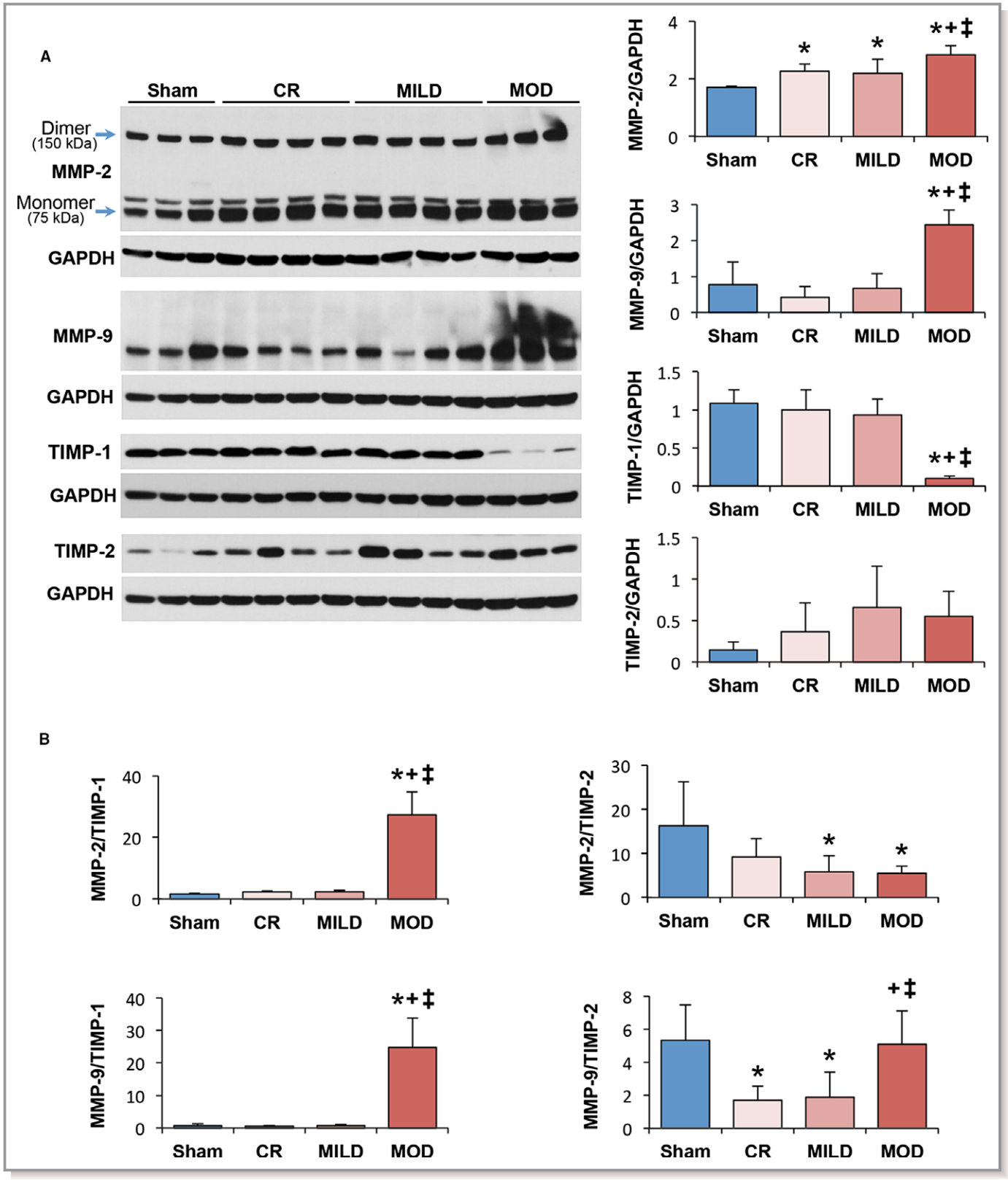

Figure 5. Assessment of the matrix metalloproteinases (MMP) and their tissue inhibitors (TIMP) in the different phenotypes. A, MMP-2, MMP-9, TIMP-1, and TIMP-2 expression in the different phenotypes compared to sham. Blue arrows showing MMP-2 monomer and dimer at 75 and 150 kDa, respectively. B, Ratios of MMP-2 and MMP-9 over TIMP-1 and TIMP-2, respectively. The n number of animals studied for immunoblotting in the sham, CR, MILD, and MOD groups is 5, 8, 8, and 6, respectively. Bar graphs show mean and SD. *P<0.05 vs sham; ^{+}P<0.05 vs CR and $^{\ddagger}P$<0.05 vs MILD. CR indicates concentric remodeling; MILD, mild eccentric remodeling; MOD, moderate eccentric remodeling.

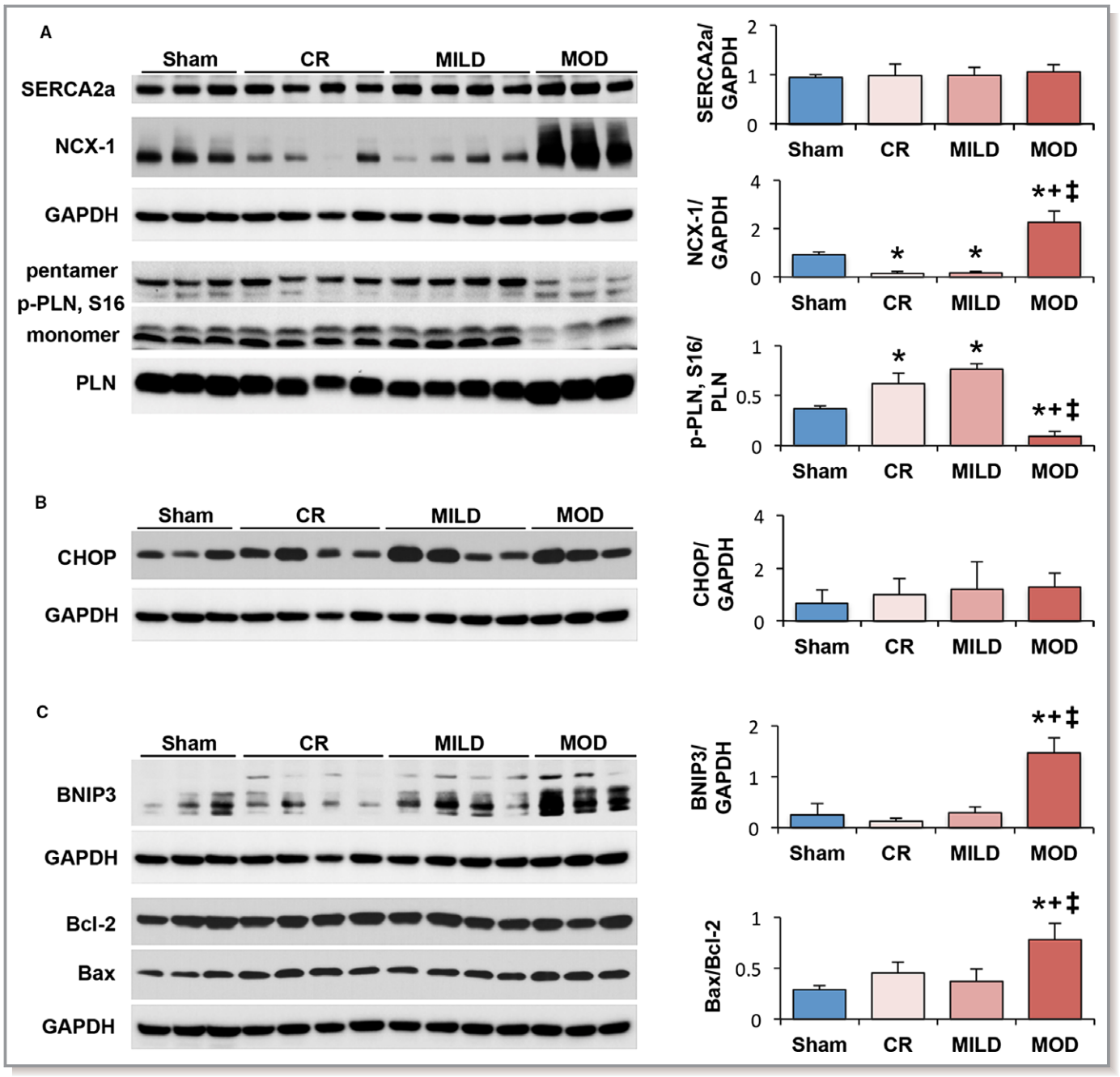

Figure 6. Assessment of calcium cycling proteins, endoplasmic reticulum stress apoptotic and mitochondrial pro-apoptotic markers, biogenesis, and content in the different phenotypes. A, SERCA2a and NCX-1 expression and ratio of S16 phosphorylated to total phospholamban. B, CHOP expression. C, BNIP3 expression and Bax/Bcl-2 ratio in the different phenotypes compared to sham. The n number of animals studied for immunoblotting in the sham, CR, MILD, and MOD groups is 5, 8, 8, and 6, respectively. Bar graphs show mean and SD. *P<0.05 vs sham; ^{+}P<0.05 vs CR and $^{\ddagger}P$<0.05 vs MILD. CR indicates concentric remodeling; MILD, mild eccentric remodeling; MOD, moderate eccentric remodeling.

influence response to POL, these factors were not operative in our study and rats of similar age and size (180–200 g) were used. Lastly, our use of AAB rather than the transverse AB minimizes variability related to branch vessel circulation variation (but precludes measurement of transband gradient).

Pathological hypertrophic remodeling is characterized by altered calcium handling, changes in metabolic pattern and fetal gene expression, enhanced apoptosis and autophagy, and extracellular matrix remodeling.[32,33] These processes are the result of altered signaling induced by cell-membrane sensors, mainly G-proteins and strain-sensitive cellular elements that translate cardiac stress into response pathways.[32,33] The end product is enhanced activity of kinases and phosphatases, such as calcineurin,[34,35] protein kinase

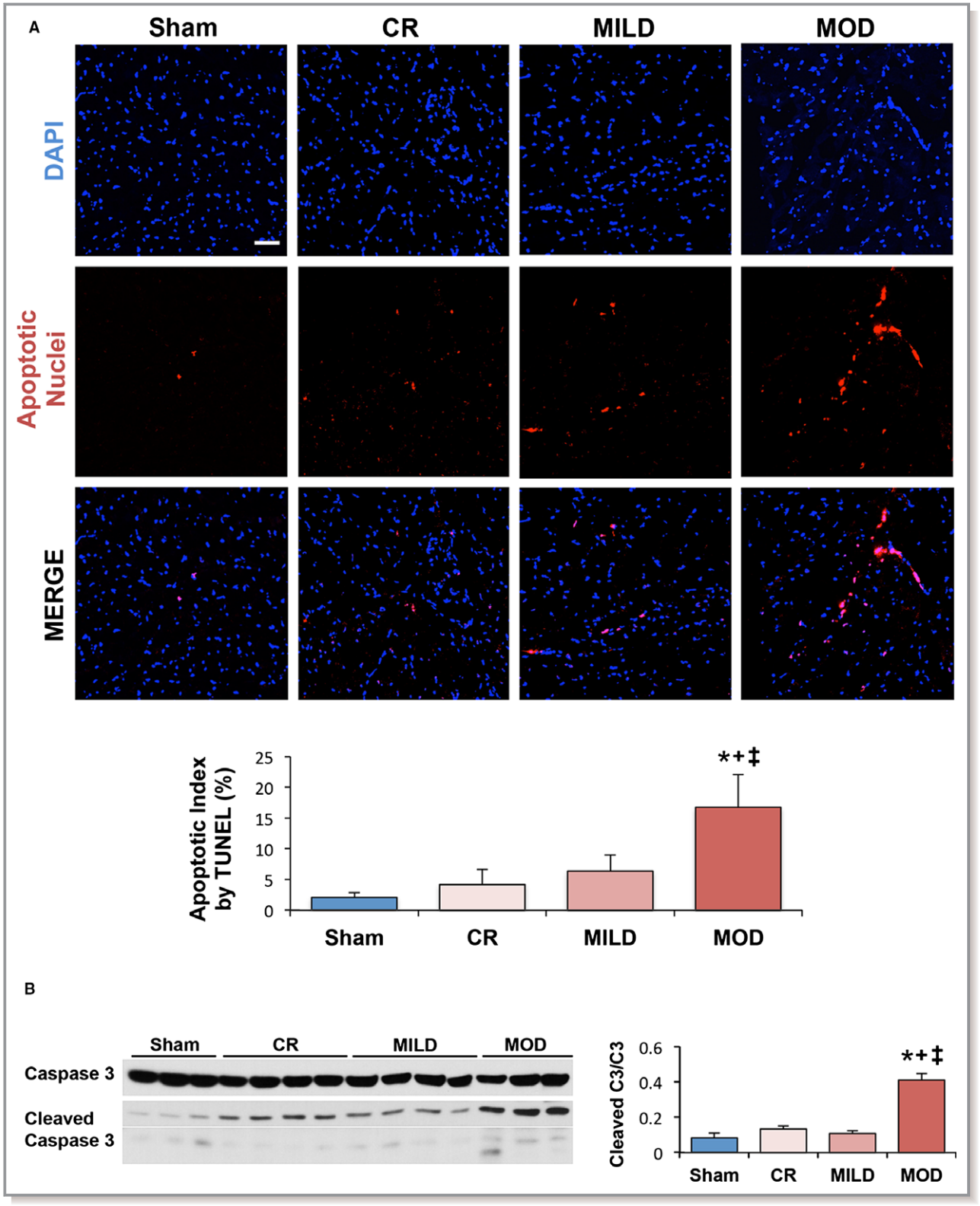

Figure 7. Assessment of apoptosis in the different phenotypes. A, TUNEL assay in the different phenotypes compared to sham. Images are 20× magnified, scale bar = 50 μm. The n number of studied animals for sham, CR, MILD, and MOD is 5, 8, 8, and 7, respectively. B, Cleaved caspase 3 relative to caspase 3 expression in the different phenotypes compared with sham. The n number of studied animals in the sham, CR, MILD, and MOD is 5, 8, 8, and 6, respectively. Bar graphs show mean and standard deviation. $^{*}P<0.05$ vs sham; $^{+}P<0.05$ vs CR and $^{‡}P<0.05$ vs MILD. CR indicates concentric remodeling; MILD, mild eccentric remodeling; MOD, moderate eccentric remodeling; TUNEL, terminal deoxynucleotidyl transferase-mediated dUTP-biotin nick-end labeling.

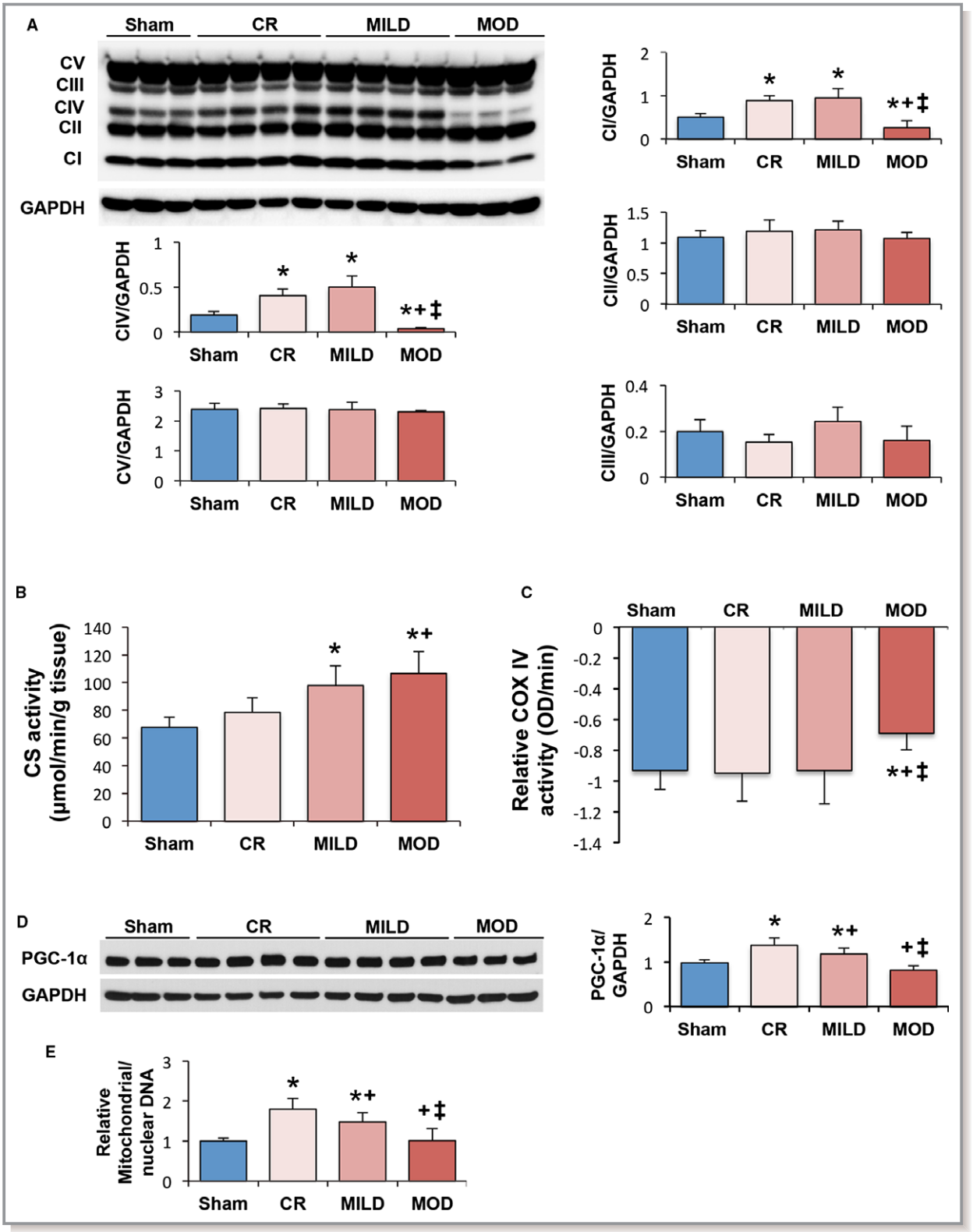

Figure 8. Assessment of mitochondrial oxidative phosphorylation in the different phenotypes. A, Electron transport chain complexes I–V. B, Citrate synthase (CS) activity. C, COX IV activity. D, PGC-1α expression. E, Mitochondrial to nuclear DNA ratio across the different phenotypes relative to sham. The n number of studied animals for sham, CR, MILD, and MOD is 5, 8, 8, and 6 for immunoblotting and 5, 8, 8, and 7 for CS and COX IV activity, respectively. Bar graphs show mean and SD. *P<0.05 vs sham; ^{+}P<0.05 vs CR and $^{‡}P$<0.05 vs MILD. CR indicates concentric remodeling; MILD, mild eccentric remodeling; MOD, moderate eccentric remodeling.

A[36] (activated initially with later decreases in activity) and C,[37] calcium-calmodulin-dependent kinase II[38,39] and the mitogen-activated protein kinases.[12] Calcineurin dephosphorylates the nuclear factor of activated T cells, which then translocates to the nucleus, interacts with the cardiac zinc finger transcription factor (GATA4),[34] and orchestrates the reactivation of fetal genes such as natriuretic peptides and alpha-skeletal muscle actin, which were increased in all phenotypes here. Calcineurin also activates protein kinase C,[40] and activated protein kinase C in cardiac stress[37] phosphorylates and inhibits inhibitor 1, leading to phospholamban dephosphorylation and inhibition of SERCA2a activity. Interestingly, despite enhanced expression of fetal genes in all phenotypes, p-phospholamban, S16 was increased in the CR and MILD phenotypes and decreased in the MOD phenotype only. Thus, the MOD phenotype displayed features shown in other studies, where the transition from compensated hypertrophy to overt HF is characterized by increased calcium-calmodulin-dependent kinase II activity and decreased PKA phosphorylation of downstream targets leading to increased sarcoplasmic reticulum Ca^{2+} leak, reduced sarcoplasmic reticulum Ca^{2+} load, and therefore impaired systolic Ca^{2+} transients.[36] Similarly, the expression of NCX-1, which is regulated by the mitogen-activated protein kinases P38 and HDAC,[41,42] and mitochondrial apoptosis markers (Bax and BNIP3), which are regulated by the mitogen-activated protein kinases JNK,[12] were increased in the MOD phenotype only. These findings suggest that despite preservation of LVEF (relative to sham), the MOD phenotype had differential activation of signaling pathways and/or degradation systems[43] than the CR and MILD phenotypes and similar to that seen in systolic HF.

Perturbations in mitochondrial homeostasis and function and metabolic remodeling occupy a central role in the pathophysiology of HF.[44,45] Prior studies indicate that mitochondrial biogenesis, signaling, and oxidative capacity are preserved or increased in early stages of compensated hypertrophy in order to match the increased energy demand imposed by enhanced workload,[46] as was the case in the CR and MILD phenotypes. The transition to HF has been reported to be preceded or paralleled by decreases in mitochondrial biogenesis and oxidative metabolism,[46,47] as was the case in the MOD phenotype. However, definitive data to prove that mitochondrial dysfunction causes the transition from compensated hypertrophy to HF are lacking. Here, we observed that the transition from CR to MILD phenotype was accompanied by decrease in PGC-1α expression and mitochondrial content with no change in mitochondrial oxidative capacity, whereas the MOD phenotype showed return of mitochondrial biogenesis and content markers to baseline (sham) levels and enhanced mitophagy in the face of escalating energetic demand (wall stress) as well as the development of impaired oxidative capacity, despite preservation in LVEF. This observation suggests early compensatory enhancement in mitochondrial homeostasis but that impairment in mitochondrial homeostasis and function develops and precedes the development of overt systolic dysfunction in concert with progressive ER. This is in line with what has been shown in children with right ventricular failure secondary to congenital heart disease[48] and in mice with myocardial remodeling and failure postinfarction.[49] It has been shown that PGC-1α controls mitochondrial density[50] and fatty acid oxidation[51,52] and its amount directly correlates with mitochondrial density, oxidative capacity,[47] and the metabolic shift from fatty acid oxidation to glucose oxidation,[51] which precedes cardiac decompensation.[46] Previous studies assessing changes in the expression and activity of the ETC complexes in HF have shown variable results, and such changes may vary according to the HF model.[45] Specifically, complex IV expression and COX IV activity were shown to be decreased in experimental POL-induced systolic HF and in humans with systolic HF.[53,54] Here we observed decreases in complex I and complex IV expression and COX IV activity in the MOD phenotype. The changes in ETC complexes in the MOD phenotype appeared out of proportion to the level of decrease in PGC-1α expression, which was similar to sham, suggesting that other factors may be involved in disruption of ETC such as mitochondrial Ca^{2+} overload and increased reactive oxygen species (ROS), both previously reported in the AAB model.[49,55] Moreover, CS activity increased progressively despite the progressive decrease in mitochondrial biogenesis and content across the 3 phenotypes. This is in contrast to what has been shown in systolic HF where CS activity is decreased along with the decrease in mitochondrial biogenesis and content.[47] This may suggest that the decrease in CS activity occurs later in the progression to overt systolic dysfunction and HF.

The absence of a treatment arm poses a major limitation to our study; however, the data presented highlight some of the many complex pathophysiological processes that are involved in myocardial remodeling and are activated before the transition to overt systolic HF. Specifically, we showed that alterations in calcium handling, MMP expression and regulation, mitochondrial integrity, and oxidative capacity as well as enhanced apoptosis and autophagy were activated before the onset of overt systolic HF and correlated with myocardial remodeling despite the preservation of LVEF. This study provides evidence that future studies should aim at targeting the disease at an earlier stage rather than when the full-blown systolic HF phenotype ensues. The MOD phenotype constitutes a suitable and an appealing animal model to study potential antiremodeling therapies at an earlier stage of HF in the future. Moreover, and given the complexity of the aforementioned pathophysiological processes, identifying targets that are able to simultaneously modulate 2 or more

of the pathophysiological processes involved in HF may stand a better chance at achieving a more desirable long-term effect.

Our study has other limitations. We did not study rats with the 3 phenotypes at later time points to determine whether there is consistent but time-dependent progression to more severe ER and mitochondrial disruption with this model. The assessment of mitochondrial oxidative capacity by measuring CS and COX IV activity from frozen tissue is a limitation. Future studies using high-resolution respirometry in isolated mitochondria are needed to confirm and extend our findings. While LV peak systolic pressure at terminal study was similar across phenotypes and the modest differences in LV volume and LVEF would suggest similar stroke volumes across the 3 phenotypes, we cannot exclude differences in transband gradient in the 3 phenotypes. If such (likely) modest differences were critical to our observations, a highly specific stress set point for triggering pathologic hypertrophic remodeling would be suggested. This is unlikely given that phenotypic variability was also seen in studies using a tighter vascular clip.[11] Differences in activity among animals may contribute to the cumulative severity of cardiac stress and contribute to variability, but activity patterns were not assessed.

In conclusion, it remains unclear what triggers and initiates these signal transduction differences, but it is very clear and well evident that changes in signaling, calcium handling, and mitochondrial homeostasis and function correlate with the degree of myocardial remodeling and precede the development of systolic HF.

Sources of Funding

This work is supported by the NIH R01 HL105418-01A1-04, HL76611-10CB, and HL7661-10P1 (to Redfield). Guenzel was supported by the Cardiovasology training grant 4T32HL007111-39.

Disclosures

None.

References

1. McMurray JJ, Petrie MC, Murdoch DR, Davie AP. Clinical epidemiology of heart failure: public and private health burden. *Eur Heart J*. 1998;19(Suppl P):P9–P16.
2. Nichols M, Townsend N, Scarborough P, Rayner M. Cardiovascular disease in Europe 2014: epidemiological update. *Eur Heart J*. 2014;35:2950–2959.
3. Williamson JD, Supiano MA, Applegate WB, Berlowitz DR, Campbell RC, Chertow GM, Fine LJ, Haley WE, Hawfield AT, Ix JH, Kitzman DW, Kostis JB, Krousel-Wood MA, Launer LJ, Oparil S, Rodriguez CJ, Roumie CL, Shorr RI, Sink KM, Wadley VG, Whelton PK, Whittle J, Woolard NF, Wright JT Jr, Pajewski NM. Intensive vs standard blood pressure control and cardiovascular disease outcomes in adults aged >/=75 years: a randomized clinical trial. *JAMA*. 2016;315:2673–2682.
4. Thomopoulos C, Parati G, Zanchetti A. Effects of blood pressure-lowering treatment. 6. Prevention of heart failure and new-onset heart failure–meta-analyses of randomized trials. *J Hypertens* 2016;34:373–384; discussion 384.
5. Roger VL. Epidemiology of heart failure. *Circ Res*. 2013;113:646–659.
6. Barrick CJ, Dong A, Waikel R, Corn D, Yang F, Threadgill DW, Smyth SS. Parent-of-origin effects on cardiac response to pressure overload in mice. *Am J Physiol Heart Circ Physiol*. 2009;297:H1003–H1009.
7. Barrick CJ, Rojas M, Schoonhoven R, Smyth SS, Threadgill DW. Cardiac response to pressure overload in 129S1/SvimJ and C57BL/6J mice: temporal- and background-dependent development of concentric left ventricular hypertrophy. *Am J Physiol Heart Circ Physiol*. 2007;292:H2119–H2130.
8. Lygate CA, Schneider JE, Hulbert K, ten Hove M, Sebag-Montefiore LM, Cassidy PJ, Clarke K, Neubauer S. Serial high resolution 3D-MRI after aortic banding in mice: band internalization is a source of variability in the hypertrophic response. *Basic Res Cardiol*. 2006;101:8–16.
9. Mohammed SF, Storlie JR, Oehler EA, Bowen LA, Korinek J, Lam CS, Simari RD, Burnett JC Jr, Redfield MM. Variable phenotype in murine transverse aortic constriction. *Cardiovasc Pathol*. 2012;21:188–198.
10. Del Monte F, Butler K, Boecker W, Gwathmey JK, Hajjar RJ. Novel technique of aortic banding followed by gene transfer during hypertrophy and heart failure. *Physiol Genomics*. 2002;9:49–56.
11. Chaanine AH, Gordon RE, Kohlbrenner E, Benard L, Jeong D, Hajjar RJ. Potential role of BNIP3 in cardiac remodeling, myocardial stiffness, and endoplasmic reticulum: mitochondrial calcium homeostasis in diastolic and systolic heart failure. *Circ Heart Fail*. 2013;6:572–583.
12. Chaanine AH, Jeong D, Liang L, Chemaly ER, Fish K, Gordon RE, Hajjar RJ. JNK modulates FOXO3a for the expression of the mitochondrial death and mitophagy marker BNIP3 in pathological hypertrophy and in heart failure. *Cell Death Dis*. 2012;3:265.
13. Pacher P, Nagayama T, Mukhopadhyay P, Batkai S, Kass DA. Measurement of cardiac function using pressure-volume conductance catheter technique in mice and rats. *Nat Protoc*. 2008;3:1422–1434.
14. Mannaerts HF, van der Heide JA, Kamp O, Stoel MG, Twisk J, Visser CA. Early identification of left ventricular remodelling after myocardial infarction, assessed by transthoracic 3D echocardiography. *Eur Heart J*. 2004;25:680–687.
15. Bolognese L, Neskovic AN, Parodi G, Cerisano G, Buonamici P, Santoro GM, Antoniucci D. Left ventricular remodeling after primary coronary angioplasty: patterns of left ventricular dilation and long-term prognostic implications. *Circulation*. 2002;106:2351–2357.
16. Rooney JP, Ryde IT, Sanders LH, Howlett EH, Colton MD, Germ KE, Mayer GD, Greenamyre JT, Meyer JN. PCR based determination of mitochondrial DNA copy number in multiple species. *Methods Mol Biol*. 2015;1241:23–38.
17. Alp PR, Newsholme EA, Zammit VA. Activities of citrate synthase and NAD+-linked and NADP+-linked isocitrate dehydrogenase in muscle from vertebrates and invertebrates. *Biochem J*. 1976;154:689–700.
18. Rooyackers OE, Senden JM, Soeters PB, Saris WH, Wagenmakers AJ. Prolonged activation of the branched-chain alpha-keto acid dehydrogenase complex in muscle of zymosan treated rats. *Eur J Clin Invest*. 1995;25:548–552.
19. Li YY, Feldman AM, Sun Y, McTiernan CF. Differential expression of tissue inhibitors of metalloproteinases in the failing human heart. *Circulation*. 1998;98:1728–1734.
20. Paolocci N, Tavazzi B, Biondi R, Gluzband YA, Amorini AM, Tocchetti CG, Hejazi M, Caturegli PM, Kajstura J, Lazzarino G, Kass DA. Metalloproteinase inhibitor counters high-energy phosphate depletion and amp deaminase activity enhancing ventricular diastolic compliance in subacute heart failure. *J Pharmacol Exp Ther*. 2006;317:506–513.
21. Polyakova V, Hein S, Kostin S, Ziegelhoeffer T, Schaper J. Matrix metalloproteinases and their tissue inhibitors in pressure-overloaded human myocardium during heart failure progression. *J Am Coll Cardiol* 2004;44:1609–1618.
22. Spinale FG. Matrix metalloproteinases: regulation and dysregulation in the failing heart. *Circ Res*. 2002;90:520–530.
23. Heymans S, Schroen B, Vermeersch P, Milting H, Gao F, Kassner A, Gillijns H, Herijgers P, Flameng W, Carmeliet P, Van de Werf F, Pinto YM, Janssens S. Increased cardiac expression of tissue inhibitor of metalloproteinase-1 and tissue inhibitor of metalloproteinase-2 is related to cardiac fibrosis and dysfunction in the chronic pressure-overloaded human heart. *Circulation*. 2005;112:1136–1144.
24. Koo BH, Kim YH, Han JH, Kim DS. Dimerization of matrix metalloproteinase-2 (MMP-2): functional implication in MMP-2 activation. *J Biol Chem*. 2012;287:22643–22653.
25. Schillinger W, Schneider H, Minami K, Ferrari R, Hasenfuss G. Importance of sympathetic activation for the expression of Na+-Ca2+ exchanger in end-stage failing human myocardium. *Eur Heart J*. 2002;23:1118–1124.
26. Roos KP, Jordan MC, Fishbein MC, Ritter MR, Friedlander M, Chang HC, Rahgozar P, Han T, Garcia AJ, Maclellan WR, Ross RS, Philipson KD.

Hypertrophy and heart failure in mice overexpressing the cardiac sodium-calcium exchanger. *J Card Fail*. 2007;13:318–329.

27. Sande JB, Sjaastad I, Hoen IB, Bokenes J, Tonnessen T, Holt E, Lunde PK, Christensen G. Reduced level of serine(16) phosphorylated phospholamban in the failing rat myocardium: a major contributor to reduced SERCA2 activity. *Cardiovasc Res*. 2002;53:382–391.
28. Hu ST, Liu GS, Shen YF, Wang YL, Tang Y, Yang YJ. Defective Ca(2+) handling proteins regulation during heart failure. *Physiol Res*. 2011;60:27–37.
29. Brixius K, Wollmer A, Bolck B, Mehlhorn U, Schwinger RH. Ser16-, but not Thr17-phosphorylation of phospholamban influences frequency-dependent force generation in human myocardium. *Pflugers Arch*. 2003;447:150–157.
30. Fu HY, Okada K, Liao Y, Tsukamoto O, Isomura T, Asai M, Sawada T, Okuda K, Asano Y, Sanada S, Asanuma H, Asakura M, Takashima S, Komuro I, Kitakaze M, Minamino T. Ablation of C/EBP homologous protein attenuates endoplasmic reticulum-mediated apoptosis and cardiac dysfunction induced by pressure overload. *Circulation*. 2010;122:361–369.
31. Skavdahl M, Steenbergen C, Clark J, Myers P, Demianenko T, Mao L, Rockman HA, Korach KS, Murphy E. Estrogen receptor-beta mediates male-female differences in the development of pressure overload hypertrophy. *Am J Physiol Heart Circ Physiol*. 2005;288:H469–H476.
32. Hill JA, Olson EN. Cardiac plasticity. *N Engl J Med*. 2008;358:1370–1380.
33. Kehat I, Molkentin JD. Molecular pathways underlying cardiac remodeling during pathophysiological stimulation. *Circulation*. 2010;122:2727–2735.
34. Molkentin JD, Lu JR, Antos CL, Markham B, Richardson J, Robbins J, Grant SR, Olson EN. A calcineurin-dependent transcriptional pathway for cardiac hypertrophy. *Cell*. 1998;93:215–228.
35. Bueno OF, Wilkins BJ, Tymitz KM, Glascock BJ, Kimball TF, Lorenz JN, Molkentin JD. Impaired cardiac hypertrophic response in calcineurin abeta -deficient mice. *Proc Natl Acad Sci USA*. 2002;99:4586–4591.
36. Fischer TH, Herting J, Tirilomis T, Renner A, Neef S, Toischer K, Ellenberger D, Forster A, Schmitto JD, Gummert J, Schondube FA, Hasenfuss G, Maier LS, Sossalla S. Ca2+/calmodulin-dependent protein kinase ii and protein kinase a differentially regulate sarcoplasmic reticulum Ca2+ leak in human cardiac pathology. *Circulation*. 2013;128:970–981.
37. Braz JC, Gregory K, Pathak A, Zhao W, Sahin B, Klevitsky R, Kimball TF, Lorenz JN, Nairn AC, Liggett SB, Bodi I, Wang S, Schwartz A, Lakatta EG, DePaoli-Roach AA, Robbins J, Hewett TE, Bibb JA, Westfall MV, Kranias EG, Molkentin JD. PKC-alpha regulates cardiac contractility and propensity toward heart failure. *Nat Med*. 2004;10:248–254.
38. Backs J, Backs T, Neef S, Kreusser MM, Lehmann LH, Patrick DM, Grueter CE, Qi X, Richardson JA, Hill JA, Katus HA, Bassel-Duby R, Maier LS, Olson EN. The delta isoform of Cam kinase II is required for pathological cardiac hypertrophy and remodeling after pressure overload. *Proc Natl Acad Sci USA*. 2009;106:2342–2347.
39. Ling H, Zhang T, Pereira L, Means CK, Cheng H, Gu Y, Dalton ND, Peterson KL, Chen J, Bers D, Brown JH. Requirement for Ca2+/calmodulin-dependent kinase II in the transition from pressure overload-induced cardiac hypertrophy to heart failure in mice. *J Clin Invest*. 2009;119:1230–1240.
40. Shintani-Ishida K, Yoshida K. Ischemia induces phospholamban dephosphorylation via activation of calcineurin, PKC-alpha, and protein phosphatase 1, thereby inducing calcium overload in reperfusion. *Biochim Biophys Acta*. 2011;1812:743–751.
41. Menick DR, Li MS, Chernysh O, Renaud L, Kimbrough D, Kasiganesan H, Mani SK. Transcriptional pathways and potential therapeutic targets in the regulation of Ncx1 expression in cardiac hypertrophy and failure. *Adv Exp Med Biol*. 2013;961:125–135.
42. Menick DR, Renaud L, Buchholz A, Muller JG, Zhou H, Kappler CS, Kubalak SW, Conway SJ, Xu L. Regulation of Ncx1 gene expression in the normal and hypertrophic heart. *Ann N Y Acad Sci*. 2007;1099:195–203.
43. Willis MS, Townley-Tilson WH, Kang EY, Homeister JW, Patterson C. Sent to destroy: the ubiquitin proteasome system regulates cell signaling and protein quality control in cardiovascular development and disease. *Circ Res*. 2010;106:463–478.
44. Neubauer S. The failing heart–an engine out of fuel. *N Engl J Med*. 2007;356:1140–1151.
45. Rosca MG, Tandler B, Hoppel CL. Mitochondria in cardiac hypertrophy and heart failure. *J Mol Cell Cardiol*. 2013;55:31–41.
46. Doenst T, Pytel G, Schrepper A, Amorim P, Farber G, Shingu Y, Mohr FW, Schwarzer M. Decreased rates of substrate oxidation ex vivo predict the onset of heart failure and contractile dysfunction in rats with pressure overload. *Cardiovasc Res*. 2010;86:461–470.
47. Garnier A, Fortin D, Delomenie C, Momken I, Veksler V, Ventura-Clapier R. Depressed mitochondrial transcription factors and oxidative capacity in rat failing cardiac and skeletal muscles. *J Physiol*. 2003;551:491–501.
48. Karamanlidis G, Bautista-Hernandez V, Fynn-Thompson F, Del Nido P, Tian R. Impaired mitochondrial biogenesis precedes heart failure in right ventricular hypertrophy in congenital heart disease. *Circ Heart Fail*. 2011;4:707–713.
49. Ide T, Tsutsui H, Hayashidani S, Kang D, Suematsu N, Nakamura K, Utsumi H, Hamasaki N, Takeshita A. Mitochondrial DNA damage and dysfunction associated with oxidative stress in failing hearts after myocardial infarction. *Circ Res*. 2001;88:529–535.
50. Lehman JJ, Barger PM, Kovacs A, Saffitz JE, Medeiros DM, Kelly DP. Peroxisome proliferator-activated receptor gamma coactivator-1 promotes cardiac mitochondrial biogenesis. *J Clin Invest*. 2000;106:847–856.
51. Lehman JJ, Boudina S, Banke NH, Sambandam N, Han X, Young DM, Leone TC, Gross RW, Lewandowski ED, Abel ED, Kelly DP. The transcriptional coactivator PGC-1alpha is essential for maximal and efficient cardiac mitochondrial fatty acid oxidation and lipid homeostasis. *Am J Physiol Heart Circ Physiol*. 2008;295:H185–H196.
52. Riehle C, Wende AR, Zaha VG, Pires KM, Wayment B, Olsen C, Bugger H, Buchanan J, Wang X, Moreira AB, Doenst T, Medina-Gomez G, Litwin SE, Lelliott CJ, Vidal-Puig A, Abel ED. PGC-1beta deficiency accelerates the transition to heart failure in pressure overload hypertrophy. *Circ Res* 2011;109:783–793.
53. Quigley AF, Kapsa RM, Esmore D, Hale G, Byrne E. Mitochondrial respiratory chain activity in idiopathic dilated cardiomyopathy. *J Card Fail*. 2000;6:47–55.
54. Sparagna GC, Chicco AJ, Murphy RC, Bristow MR, Johnson CA, Rees ML, Maxey ML, McCune SA, Moore RL. Loss of cardiac tetralinoleoyl cardiolipin in human and experimental heart failure. *J Lipid Res*. 2007;48:1559–1570.
55. Chaanine AH, Kohlbrenner E, Gamb SI, Guenzel AJ, Klaus KA, Fayyaz AU, Nair KS, Hajjar RJ, Redfield MM. Foxo3a regulates BNIP3 and modulates mitochondrial calcium, dynamics and function in cardiac stress. *Am J Physiol Heart Circ Physiol*. 2016;311:H1540–H1559.